chemosensors

MDPI

Article

Two-Dimensional Dy_2O_3-Pd-PDA/rGO Heterojunction Nanocomposite: Synergistic Effects of Hybridisation, UV Illumination and Relative Humidity on Hydrogen Gas Sensing

Hanie Hashtroudi [1,*], Aimin Yu [1], Saulius Juodkazis [1,2] and Mahnaz Shafiei [1,*]

[1] School of Science, Computing and Engineering Technologies, Swinburne University of Technology, Melbourne 3122, Australia; aiminyu@swin.edu.au (A.Y.); ajuodkazis@swin.edu.au (S.J.)
[2] World Research Hub Initiative (WRHI), School of Materials and Chemical Technology, Institute of Technology, 2-12-1, Ookayama, Meguro-Ku, Tokyo 152-8550, Japan
* Correspondence: hhashtroudi@swin.edu.au (H.H.); mshafiei@swin.edu.au (M.S.)

Abstract: A two-dimensional (2D) Dy_2O_3-Pd-PDA/rGO heterojunction nanocomposite has been synthesised and tested for hydrogen (H_2) gas sensing under various functioning conditions, including different H_2 concentrations (50 ppm up to 6000 ppm), relative humidity (up to 25 %RH) and working temperature (up to 200 °C). The material characterisation of Dy_2O_3-Pd-PDA/rGO nanocomposite performed using various techniques confirms uniform distribution of Pd NPs and 2D Dy_2O_3 nanostructures on multi-layered porous structure of PDA/rGO nanosheets (NSs) while forming a nanocomposite. Moreover, fundamental hydrogen sensing mechanisms, including the effect of UV illumination and relative humidity (%RH), are investigated. It is observed that the sensing performance is improved as the operating temperature increases from room temperature (RT = 30 °C) to the optimum temperature of 150 °C. The humidity effect investigation revealed a drastic enhancement in sensing parameters as the %RH increased up to 20%. The highest response was found to be 145.2% towards 5000 ppm H_2 at 150 °C and 20 %RH under UV illumination (365 nm). This work offers a highly sensitive and selective hydrogen sensor based on a novel 2D nanocomposite using an environmentally friendly and energy-saving synthesis approach, enabling us to detect hydrogen molecules experimentally down to 50 ppm.

Keywords: two-dimensional Dy_2O_3-Pd-PDA/rGO heterojunction nanocomposite; conductometric devices; hydrogen gas sensors; UV illumination; relative humidity; low operating temperature

Citation: Hashtroudi, H.; Yu, A.; Juodkazis, S.; Shafiei, M. Two-Dimensional Dy_2O_3-Pd-PDA/rGO Heterojunction Nanocomposite: Synergistic Effects of Hybridisation, UV Illumination and Relative Humidity on Hydrogen Gas Sensing. *Chemosensors* **2022**, *10*, 78. https://doi.org/10.3390/chemosensors10020078

Academic Editor: Pietro Salvo

Received: 7 January 2022
Accepted: 10 February 2022
Published: 14 February 2022

1. Introduction

Hydrogen (H_2) is a non-toxic, odourless, and colourless gas that can be used as a renewable energy source [1]. H_2 is abundant on earth in different molecular forms, including water and organic chemical compounds that contain hydrogen-carbon bonds such as hydrocarbons [2]. Since H_2 is a highly flammable and explosive gas, reliable and effective sensors must be used to strictly monitor any leakage during its production procedure, storage, transport, and usage [2]. To date, different 2D semiconducting materials, including metal oxides, transition metal dichalcogenides (TMDs), and graphene-based materials, have been used as hydrogen sensors due to their electrochemical and physical characteristics [3–6]. In general, 2D semiconductors have a high number of active sites, high surface to volume ratios, and exceptional optical and electrical properties that are frequently stimulated by a concentration of charge density near or on surfaces, resulting in enhanced sensing performance (i.e., high response, gas selectivity, fast response and recovery, and durability) [7–9]. Graphene-based materials are considered as promising hydrogen sensing candidates with low operating temperatures due to their excellent charge carrier mobility, high conductivity, and electrochemical stability [10]. However, their recovery is slow and mostly show poor selectivity due to the absence of a direct

bandgap and few dangling bonds on the surface [11]. To overcome these issues, surface modification such as functionalisation with noble metal dopants (i.e., Pd, Au, and Pt) and hybridisation with metal oxides to develop a suitable composite sensing layer have been employed [12–15]. In addition, studies have shown that utilising UV radiation can significantly improve the H_2 sensing performance of graphene-based materials [16]. Functionalising the graphene-based materials, including the reduced graphene oxide (rGO) with noble metals, facilitates the H_2 molecules dissociation in the sensing layer and forms a dipole layer on the metal surface [13,17,18].

Thus, in this work we decided to combine Pd nanoparticles (NPs) with rGO nanosheets (NSs) to maximise the electro-catalytic activities [19]. Still, the spontaneous agglomeration of rGO NSs prepared by the traditional oxidation of graphite technique limits the anchor sites for Pd NPs growth. Another drawback of using the conventional methods to reduce the GO is using toxic chemicals, which produces hazardous residues that are harmful to the environment on an industrial scale [20]. Dopamine (DA) is an environmentally friendly chemical that has been used for the reduction and functionalisation of GO since 2010 [21]. The reduction process occurs when the DA starts self-polymerisation to form polydopamine (PDA) in the presence of GO oxygen functional groups in the weak alkaline pH environment, with the catechol groups undergoing oxidation until producing the quinon groups [21,22]. Therefore, to overcome all the disadvantages of traditional GO reduction methods, in this work, the GO has been reduced and functionalised by Pd NPs using a green approach with DA through a facile wet chemical process to achieve a high quality Pd-PDA/rGO nanocomposite [21].

Recently, rare earth metal oxides have also attracted considerable attention based on their thermal, physical, and chemical properties [23]. Among them, dysprosium oxide (Dy_2O_3) is a stable C-type rare-earth sesquioxide structured metal oxide that generally exists in two monoclinic and hexagonal structures [24]. It shows excellent physical and chemical properties based on its high surface to volume ratios, thermal stability, and, more importantly, by having a number of electrons in its 4f subshell [25]. Dy_2O_3 has been used in many applications, including pH sensors [25], magneto-optical memory materials [26], and gas storage [27]. He et al. [28] reported the catalytic behaviour of Dy_2O_3, which is based on its high hydrogen adsorption capability and being able to create new active sites through the hydrogen spill-over process. This proves that Dy_2O_3 might have remarkable electrochemical properties to be used as a hydrogen gas sensing layer. However, to date, there are no studies of the hydrogen sensing performance of any Dy_2O_3-based materials, which is considered the primary motivation for the present work. In this work, GO NSs are reduced by DA and functionalised with Pd NPs and 2D Dy_2O_3 nanostructures, making heterojunction Dy_2O_3-Pd-PDA/rGO nanocomposite as the final product. The synthesis process and results of surface characteristics and hydrogen gas sensing properties of the heterojunction Dy_2O_3-Pd-PDA/rGO nanocomposite is reported here for the first time to the best of the authors' knowledge. The experimental results confirm that the fabricated sensor is highly responsive to H_2 at very low concentrations with quick response and recovery, as well as long-term stability, which can be attributed to the excellent physical and chemical characteristics of the heterojunction nanocomposite.

2. Materials and Methods

2.1. Material Synthesis and Sensor Fabrication

Two-dimensional dysprosium oxide (Dy_2O_3) dispersion with the concentration of 0.15 mg/mL was obtained from 2D Semiconductors Inc, Scottsdale, AZ, USA, and the commercially produced graphene oxide (GO) powder was purchased from JCNANO INC Advanced Materials Supplier, Nanjing, China. The other used materials for the synthesis of Dy_2O_3-Pd-PDA/rGO nanocomposite, including dopamine hydrochloride (DA), sodium borohydride ($NaBH_4$), and palladium (II) chloride ($PdCl_2$), were purchased from Sigma-Aldrich (Sydney, NSW, Australia).

The schematic synthesis process of the Dy_2O_3-Pd-PDA/rGO nanocomposite is shown in Figure 1. Dy_2O_3-Pd-PDA/rGO nanocomposite was synthesised through the facile wet chemistry method in the following steps [21,22]. At first, 10 mg of GO NSs were sonicated in 30 mL of Tris buffer (pH 8.5) for 1 h, followed by adding 10 mg of DA and a further sonication to dissolve DA completely. The reaction mixture was left under vigorous shaking conditions for 24 h. This step aims to reduce the GO and functionalised it with PDA through the self-polymerisation process. The synthesised PDA/rGO nanocomposite was collected after centrifugation and washed several times with deionised water (DI). Afterwards, 1 mL of PDA/rGO (1 mg/mL) was added to a mixture comprised of 3 mL of DI water and 1 mL of $PdCl_2$ solution (5 mg/mL) and mixed thoroughly for 2 h. Then, 1 mL freshly made $NaBH_4$ solution (0.5 M) was added and stirred for 5 h. The Pd-PDA/rGO nanocomposite was collected via centrifugation and washed three times with DI water [22]. Afterwards, 0.5 mL of Pd-PDA/rGO dispersion (1 mg/mL) and 0.1 mL of Dy_2O_3 (0.15 mg/mL) was mixed for 4 h for the immobilization of Dy_2O_3 onto Pd-PDA/RGO nanocomposite. The final product of Dy_2O_3-Pd-PDA/rGO nanocomposite was collected using centrifugation and washed thoroughly three times by DI water. Then, 0.5 mL of DI was added to the final powder to make a dispersion. Subsequently, the dispersion was drop-casted onto a 10 mm × 6 mm gold interdigitated electrode fingers with a spacing of ~10 µm to make the final sensor device.

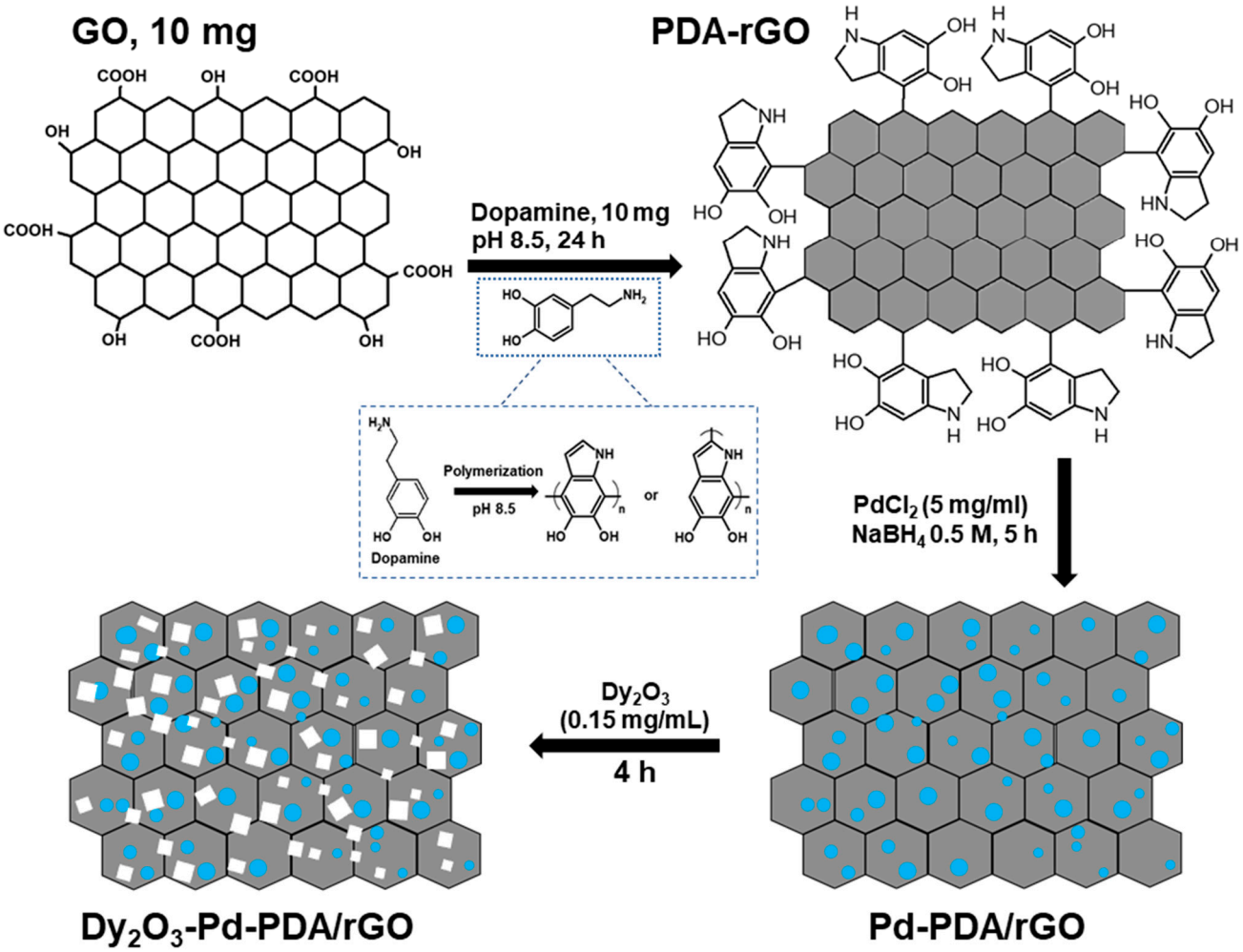

Figure 1. Schematic diagram of the synthesis process of the Dy_2O_3-Pd-PDA/rGO nanocomposite.

2.2. Material Characterisation

Different techniques were applied to analyse the structural and morphological characteristics of the synthesised Dy_2O_3-Pd-PDA/rGO nanocomposite. The surface morphology

and elemental composition of the nanocomposite were investigated using a scanning electron microscope (EBL-SEM, Raith150 Two, Dortmund, Germany, at different magnifications, an energy-dispersive X-ray spectroscope (EDS, TESCAN MIRA3 FEG-SEM combined with Thermo Scientific UltraDry EDS) (Corporation Park, VIC, Australia), and a high-resolution transmission electron microscope (HRTEM, JEOL ARM200F' NeoARM'at 200 kV, Tokyo, Japan). The crystal phases of the samples were investigated using an X-ray diffractometer (D8-Advanced, Bruker, Germany) with Cu K_α and λ = 1.54 Å at 40 kV and 20 mA over a range of 5–95 degrees. A small amount of the dried Dy_2O_3-Pd-PDA/rGO nanocomposite powder was added to ethanol, then dispersed on a carbon-coated 300 mesh copper TEM grid and allowed to dry in air at RT for the HRTEM characterisation. The Raman spectra measurements of the sample were carried out using the Raman spectroscopy (Renishaw plc, Gloucestershire, UK) excited by a 514.5 nm laser.

2.3. Hydrogen Sensing Measurments

The gas sensing properties of the Dy_2O_3-Pd-PDA/rGO nanocomposite based conductometric sensor were investigated using a gas sensing system, as illustrated in Figure 2a. Figure 2b shows a photo of the IDTs used to fabricate the sensors. This system consists of a temperature and humidity controlled Linkam stage (T96, Linkam Scientific Instruments Ltd.) (Tadworth, UK), six mass flow controllers (GE50A MFCs) (Andover, MA, USA), to regulate the gas concentrations, a humidity generator, and a built-in heater (LNP96) (Tadworth, UK). A 365 nm UV LED (Harrison, NJ, USA), (M365D1 LED, with 8.9 $\mu W/mm^2$ power-driven with a current of 700 mA) was integrated on top of the stage with a distance of 1 cm from the sensor during the experiments [8]. Different operating temperatures from RT (30 °C) to 200 °C, relative humidity from 0 to ~25 %RH at 150 °C, and hydrogen concentration from 50 to 10,000 ppm were tested. The selectivity was determined by exposing the sensor to 50 ppm of different gases, including hydrogen, acetone, ammonia, and nitrogen dioxide.

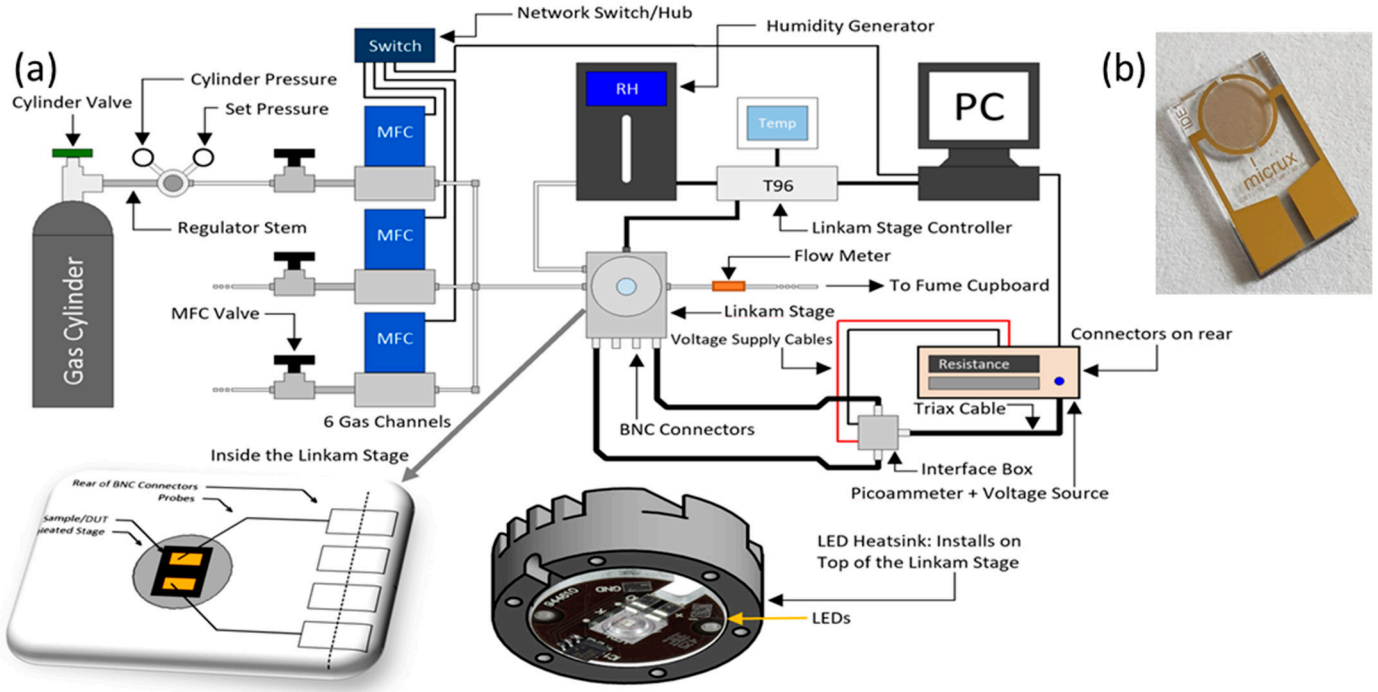

Figure 2. (**a**) Schematic diagram of the gas sensing system. Adapted with permission [8]. (**b**) A photo of the IDTs used for the fabricated sensors.

Hydrogen gas (0.1% and 1%) balanced in synthetic air with different concentrations at a uniform flow rate of 200 sccm were generated using dry synthetic air as a reference gas and the MFCs. Gas exposure time for each experiment was 15 min, followed by 2 h of

purging with synthetic air. A Keithley Piccoammeter (model 6487) (Cleveland, OH, USA) periodically measured interval currents throughout the experiments. A change in sensor resistivity was measured upon exposure to the target gas at a bias voltage of 1 V and was correlated to the gas concentrations. The sensors response (R) towards a target gas was calculated as below:

$$R = \left(\frac{R_g}{R_a}\right) \times 100, \quad (1)$$

where R_a is the resistivity of the sensor in air and R_g is the resistivity in the target analyte. The response time is considered when the sensor reaches 90% of the response, and the recovery time is calculated when the sensor recovered 90% back to its baseline. In this work, three similar sensors were fabricated, and the sensing results were comparable. Each experiment was performed at least three times under the exact working conditions to confirm the repeatability and reliability of the sensing procedure.

3. Results and Discussion

This section may be divided by subheadings. It should provide a concise and precise description of the experimental results, their interpretation, as well as the experimental conclusions that can be drawn.

3.1. Material Characterisation

XRD pattern of Dy_2O_3-Pd-PDA/rGO nanocomposite was analysed to indicate its degree of crystallinity and is illustrated in Figure 3. A relatively broad peak at 2θ = 26.6° corresponds to (002) graphitic plane of the partially restacked rGO nanosheets. The intralayer spacing between the rGO nanosheets was calculated to be 0.33 nm by the Bragg's low [29], as follows:

$$\lambda = 2d\sin(\theta), \quad (2)$$

where λ is the X-ray beam wavelength (0.154 nm), d is the distance between the rGO NSs, and θ is the diffraction angle. In the following, the graphene layers number in rGO NSs was determined to be <3 layers from the Scherrer Equation [30], as below:

$$X = \frac{K\lambda}{\beta.\cos(\theta)}, \quad (3)$$

where X is the number of rGO layers, β is the line broadening at half the maximum intensity (FWHM), K is a dimensionless shape factor, λ is the X-ray beam wavelength, and θ is the Bragg angle.

It is also seen a sharp peak at 28.5°, which corresponds to Dy_2O_3 (222) plane. Diffraction peaks at 2θ = 20.3°, 28.5°, 33°, 35.7°, 39.6°, 43.1°, 47.7°, 56.7°, and 78° assigned to the (211), (222), (400), (411), (332), (433), (440), (611), and (622) crystalline planes, respectively clearly indicate the cubic phase of the Dy_2O_3, and the peaks fit very well with the JCPDS data card No. 78-0388 [31]. The other sharp peaks that appear at 2θ = 38.6°, 44.1°, 64.7°, and 77.75° attributed to the (111), (200), (222), and (311) planes, respectively, confirm the face-centred cubic (FCC) structure of the Pd NPs inside the rGO NSs with an average of 13 nm crystalline size, which is calculated by Scherrer (Equation (3)) and fits well to the JCPDS DATA CARD No.5-681 [22].

The surface morphology of the Dy_2O_3-Pd-PDA/rGO nanocomposite was characterised by SEM at different magnifications (Figure 4). SEM images illustrate the PDA functionalised rGO nanosheets with porous structure and some open edges, which confirms that the PDA/rGO nanosheets are entirely interconnected. Figure 4 also shows that PDA/rGO nanosheets are homogeneously decorated with Pd NPs and nanoclusters. Figure 4b,c shows that the PDA/rGO NSs structure has a crumpled and wrinkled form, and the Pd and Dy_2O_3 are dispersed on both sides of the PDA/rGO NSs. Moreover, these images confirm that Pd and Dy_2O_3 are fairly distributed on PDA/rGO NSs without substantial agglomerations.

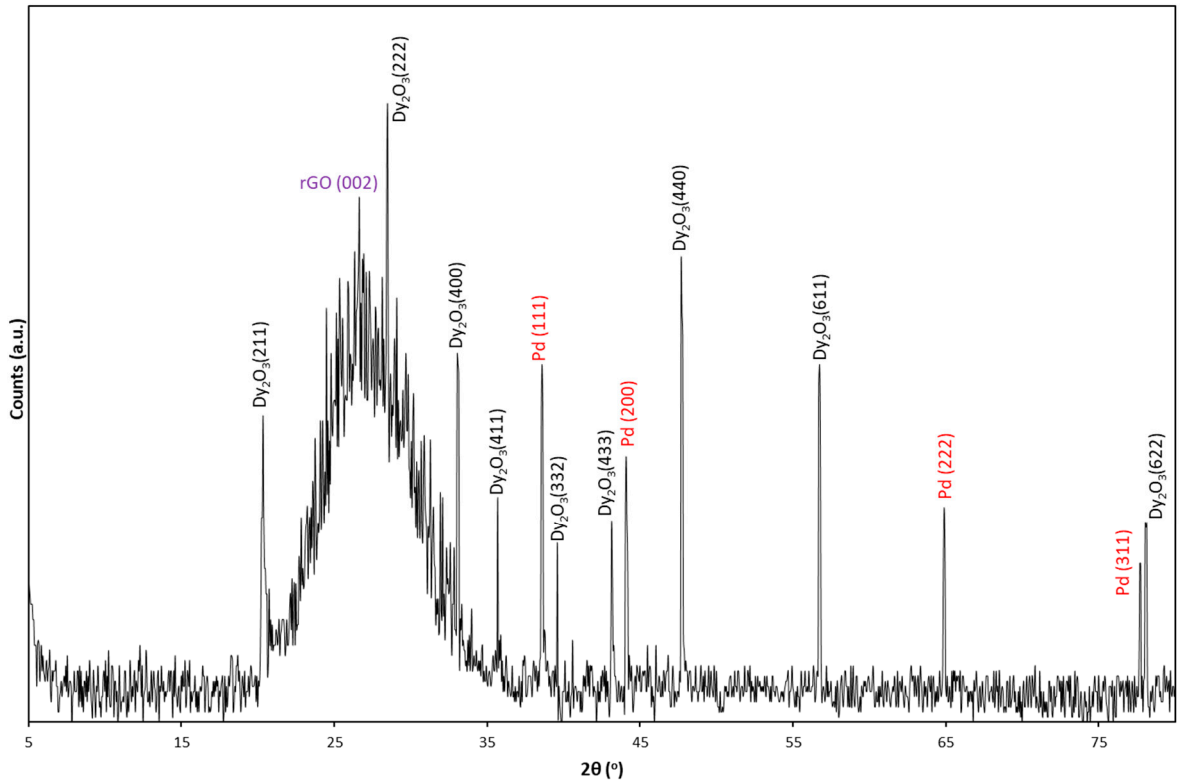

Figure 3. X-ray diffraction pattern of Dy_2O_3-Pd-PDA/rGO nanocomposite.

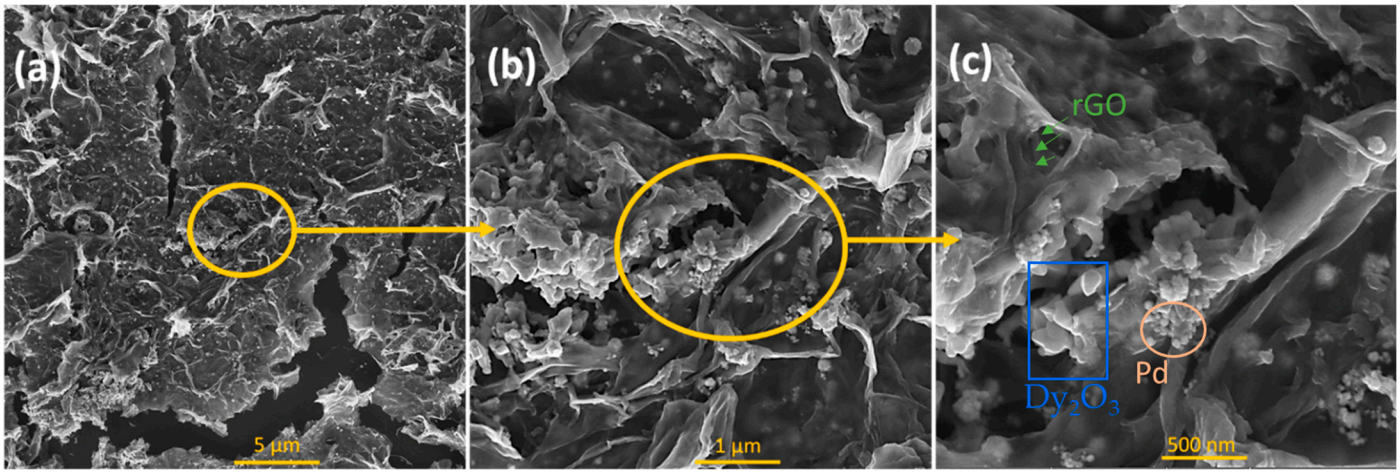

Figure 4. (**a**–**c**) SEM images of highly porous structure of Dy_2O_3-Pd-PDA/rGO nanocomposite with wrinkles and open edges at different magnifications. (**c**) shows the different elements of the nanocomposite.

Energy-dispersive X-ray spectroscopy (EDS) was also used to determine the elemental composition and surface coverage of each element on the Dy_2O_3-Pd-PDA/rGO nanocomposite (Figure 5). Figure 5b–e confirms the existence of carbon, oxygen, palladium, and dysprosium, respectively, which indicates the successful formation of Dy_2O_3-Pd-PDA/rGO nanocomposite. Figure 5f illustrates the elemental composition of the Dy_2O_3-Pd-PDA/rGO nanocomposite, confirming the Weight% and Atom% of each element.

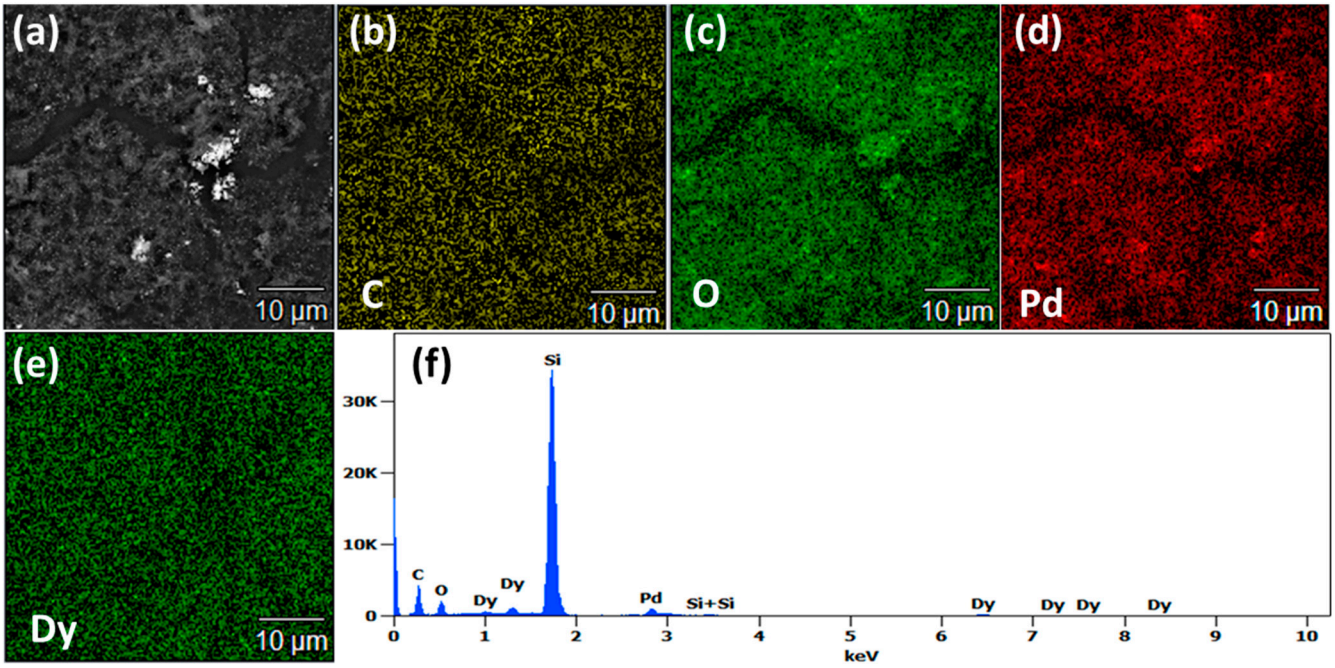

Figure 5. EDS image (**a**) and mapping of (**b**) carbon, (**c**) oxygen, (**d**) palladium, and (**e**) dysprosium; and (**f**) elemental measurement of the Dy_2O_3-Pd-PDA/rGO nanocomposite.

The Dy_2O_3-Pd-PDA/rGO nanocomposite was further analysed by HRTEM to evaluate its internal morphology and crystal structural features (Figure 6). HRTM images of Dy_2O_3-Pd-PDA/rGO nanocomposite in different magnifications indicate thin and transparent film-like morphology of the PDA-rGO NSs, which confirms the formation of a few layers of highly reduced graphene oxide decorated with Pd NPs and Dy_2O_3. Figure 6a,b illustrates the morphology of each element and distribution of the 2D structured Dy_2O_3 and Pd NPs into the rGO NSs (consistent with the SEM images). Pd NPs appear to have a nearly spherical shape, which is well dispersed onto the PDA/rGO NSs surface. It also indicates that Dy_2O_3 is distributed into the PDA/rGO NSs with some agglomerations. Figure 6c show the lattice fingers of the Pd and Dy_2O_3 planes. The interplanar spacings of 0.144 nm, 0.232 nm, and 0.205 nm are ascribed to cubic Pd (222), Pd (111), and Pd (200) lattice planes, respectively. In addition, Figure 6c indicates the polycrystalline cubic structured Dy_2O_3 (400), (440), and (222) planes with characteristic spacings of 0.271 nm, 0.235 nm, and 0.313 nm, respectively. According to Bragg's law (Equation (2)), XRD analysis of the Dy_2O_3-Pd-PDA/rGO nanocomposite supports the crystal structural features found by the HRTEM investigation. As shown in Figure 6a,b, PDA/rGO NSs are relatively thin layers that help support the Pd and Dy_2O_3 nanoclusters to form the Dy_2O_3-Pd-PDA/rGO nanocomposite.

Raman measurements at RT were performed using a 514 nm laser to characterise Dy_2O_3-Pd-PDA/rGO nanocomposite, Pd-PDA/rGO, and Dy_2O_3 and determine the structural change and formation of any defects inside the synthesised materials (Figure 7). The Raman spectrum of the 2D Dy_2O_3 indicates a sharp dominant peak at ~372 cm^{-1} assigned to F_g mode, confirming its cubic phase structure as also confirmed by XRD analysis, which is consistent with the TEM results. In comparison, this peak is shifted to a lower wavelength (~368 nm) in the Dy_2O_3-Pd-PDA/rGO nanocomposite Raman spectrum attributed to the formation of structural defects and oxygen vacancies on the nanocomposite surface due to strong interaction between the Dy_2O_3 and Pd-PDA/rGO NSs, facilitating the charge transfer from the Dy_2O_3 to rGO NSs [32]. A number of low-intensity Raman bands were also observed at F_g modes, including the 462 cm^{-1} and 585 cm^{-1}, which well describes the c-type structure of the Dy_2O_3. Comparing the 2D bands of the Dy_2O_3-Pd-PDA/rGO nanocomposite (2745 cm^{-1} and 2937 cm^{-1}) and Pd-PDA/rGO (2721 cm^{-1} and 2927 cm^{-1}) reveals that there is a general shifting to higher wavenumbers in the nanocomposite as the

layer thickness increased [33]. In addition, the broadened 2D bands in the nanocomposite represent the exfoliation of the rGO NSs [32]. The 2D bands of the pure Dy_2O_3 are found to be at 2853 cm^{-1} and 2921 cm^{-1}. The Raman spectra of the Pd-PDA/rGO in Figure 7 indicate two characteristic peaks at ~1357 cm^{-1} and 1602 cm^{-1}, corresponding to the D and G bands, respectively. While the D and G bands on the Dy_2O_3-Pd-PDA/rGO Raman spectrum are slightly shifted to lower wavelengths (~1351 cm^{-1} and 1597 cm^{-1}) due to the formation of heterojunction between the Dy_2O_3 and Pd-PDA/rGO and electron transfer from Dy_2O_3 to the Pd-PDA/rGO [34]. In general, the D band is associated with the density of defects in the sp2 hybridised material, and the G band starts by active E_{2g} phonon mode of the symmetric structure in the graphite [35,36]. The presence of these two D and G bands confirms that the structure of the Pd-PDA/rGO NSs had been maintained after loading the 2D Dy_2O_3 [37]. The intensity ratio (I_D/I_G) of the D band to G band is associated with the density of defects that arises in Pd-PDA/rGO NSs due to doping with the 2D Dy_2O_3 in the formation of Dy_2O_3-Pd-PDA/rGO nanocomposite. The I_D/I_G for Pd-PDA/rGO NSs was found to be 0.99, while it increased to 1.04 for the Dy_2O_3-Pd-PDA/rGO nanocomposite due to the higher defect density in the nanocomposite and more oxygen vacancy on its surface [38]. This result confirms that the Dy_2O_3 is successfully incorporated into the Pd-PDA/rGO NSs, forming the heterojunction Dy_2O_3-Pd-PDA/rGO nanocomposite.

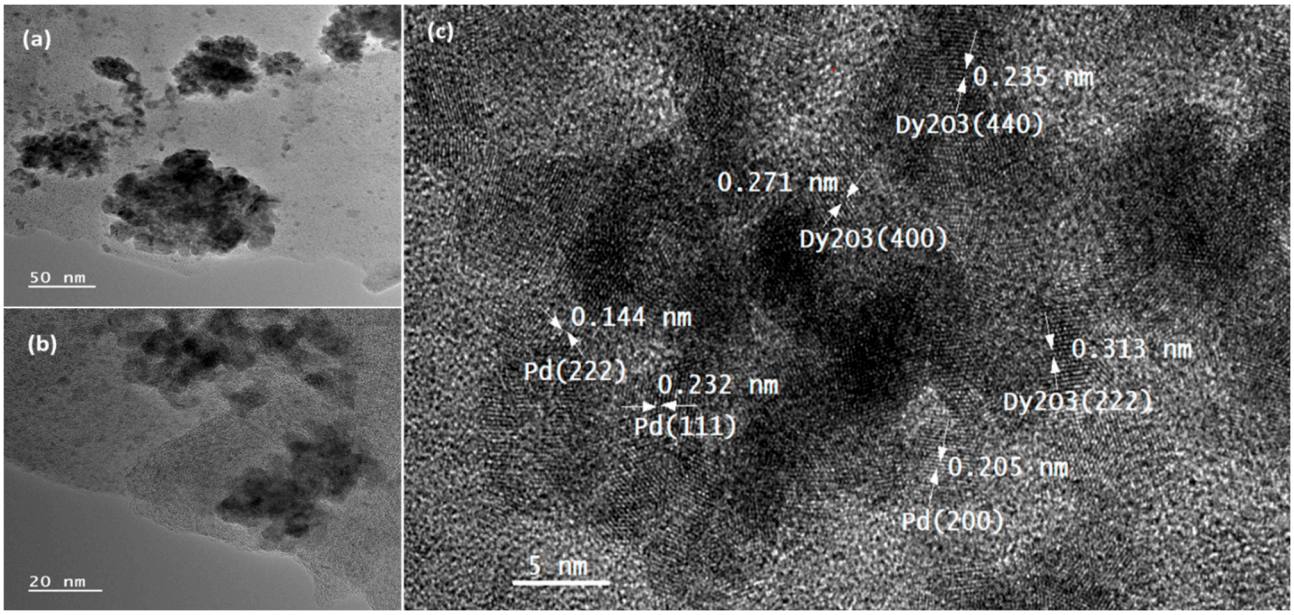

Figure 6. (**a**–**c**) HRTEM images of Dy_2O_3-Pd-PDA/rGO nanocomposite in different magnifications. (**c**) shows interplanar spacings of Pd NPs and Dy_2O_3.

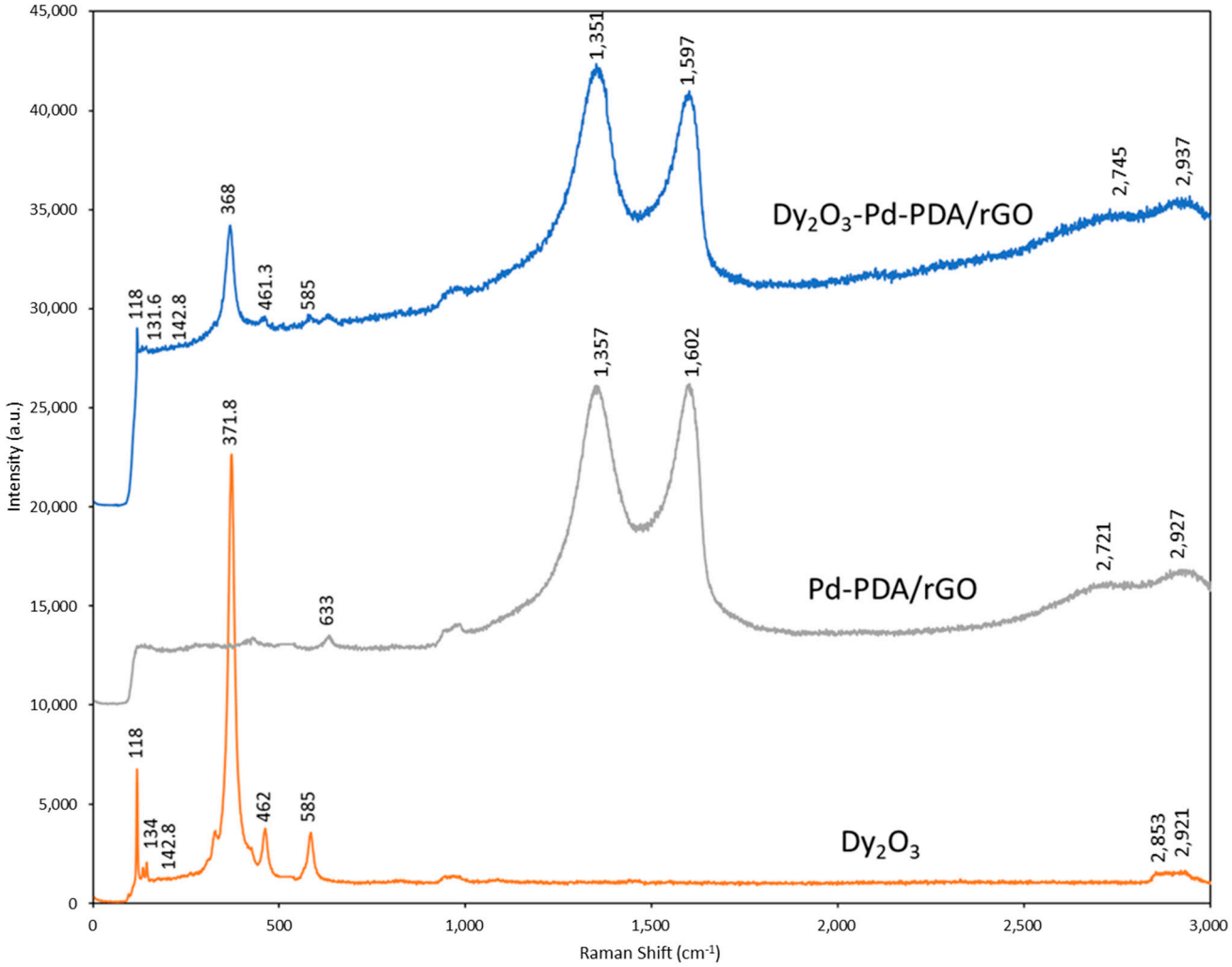

Figure 7. Raman analysis of Dy_2O_3-Pd-PDA/rGO nanocomposite, Pd-PDA/rGO, and Dy_2O_3.

3.2. Hydrogen Sensing Characterisation

The hydrogen gas sensing performance of the Dy_2O_3-Pd-PDA/rGO nanocomposite-based sensor was examined under different working conditions. The following sections report the effects of operating temperature, UV illumination, gas concentration, and humidity on the sensing parameters.

3.2.1. Effect of Working Temperature

Optimising the operating temperature is one of the critical factors in gas sensing, which directly relates to the experiment's power consumption and cost. The fabricated Dy_2O_3-Pd-PDA/rGO based conductometric sensor was examined towards 400 ppm and 600 ppm H_2 at different working temperatures under UV (365nm) illumination and 0% relative humidity (%RH). The operating temperature was changed from RT (30 °C) to 200 °C, and a change in resistivity of the sensor was monitored throughout the experiment. It was observed that the sensor's response (resistivity) increased by increasing the operating temperature from RT (30 °C) up to 150 °C, due to the acceleration of the adsorption/desorption kinetics between the H_2 molecules and the Dy_2O_3-Pd-PDA/rGO composite sensing layer [39,40]. Further increasing the operating temperature to 200 °C led to a decrease in the sensing response. This result can be attributed to the increase of the desorption rate of H_2 molecules compared to the adsorption rate while raising the temperature further than the optimum temperature, which is called the Langmuir effect [40]. Therefore, the optimum working temperature was found to be 150 °C. The 150 °C temperature corresponds to the 86 meV potential, which

is among typical overpotential values in electrochemical hydrogen evolution reaction (HER) of water splitting [41]. Figure 8a shows the typical p-type semiconducting sensing behaviour of the sensor as the conductivity decreases towards H_2 (reducing gas). The increase in the resistivity of the p-type sensor upon exposure to the reducing gas is due to the charge transfer from the target gas molecules to the sensing layer [1,41]. As an electron donor gas, H_2 transfers electrons to the valent band of the sensing layer, reducing the hole concentration on the surface, resulting in an increase in resistivity. Figure 8b illustrates the response of the sensor towards 400 and 600 ppm H_2 at different temperatures.

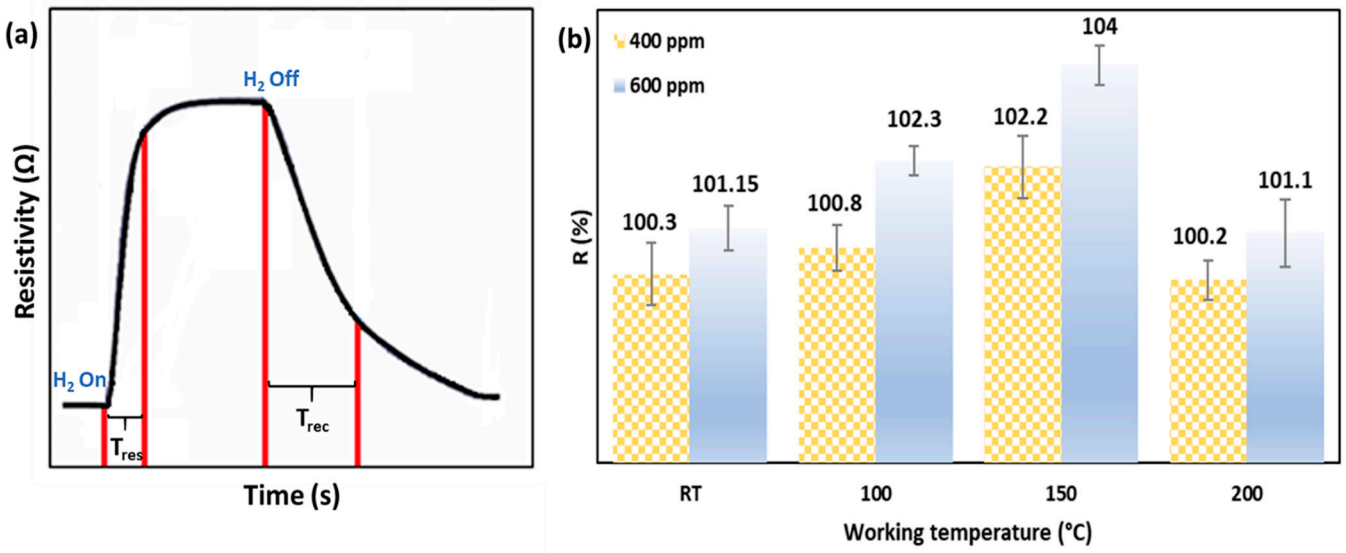

Figure 8. (**a**) P-type semiconducting sensing behaviour towards H_2 as a reducing gas, T_{res}: response time, and T_{rec}: recovery time; and (**b**) Response of the Dy_2O_3-Pd-PDA/rGO sensor towards 400 and 600 ppm hydrogen at different working temperatures.

3.2.2. Effect of UV Illumination

The effect of UV illumination on the H_2 sensing performance of the Dy_2O_3-Pd-PDA/rGO sensor was studied at 150 °C and 0 %RH as a function of hydrogen concentration. Figure 9a,b illustrate the dynamic response of the sensor towards H_2 with different concentrations (200–600 ppm) at 150 °C in the dark and under UV (365 nm) illumination, respectively. As explained in the previous section, the sensor shows a p-type semiconducting sensing behaviour as the conductivity decreases upon exposure to H_2 molecules [42]. The resistivity shifts happen based on the adsorption/desorption of the gas molecules onto the sensing layer and are correlated to the target gas concentrations [43]. This correlation could be due to the rise in gas molecules numbers interacting with the sensing layer surface. Therefore, the adsorption and desorption co-occur until the balanced state is reached [44].

As seen in Figure 9a, a baseline drift occurs without using UV illumination, indicating that the sensor cannot be fully recovered to its original baseline, showing partly reversible gas/material interactions. However, Figure 9b demonstrates fully reversible gas/material interactions under UV illumination, revealing that the sensor is fully recoverable [5,45,46]. This result can be attributed to the change of charge carrier density on the surface of the sensing layer by stimulating the electrons from the valence band of the Dy_2O_3-Pd-PDA/rGO nanocomposite while using UV radiation [47]. The desorption of H_2 molecules is accelerated by these photogenerated electrons from the pre-adsorbed ambient oxygen species [48]. In addition, the UV radiation weakens the bonding forces between the sensing layer (Dy_2O_3-Pd-PDA/rGO nanocomposite) and H_2 molecules during the physisorption, resulting in photoexcitation and reversible adsorption/desorption reactions [45,48,49]. The presence of 4f electron improves the photocatalytic activity and adsorption capacity of the Dy_2O_3 while exposed to UV. When the sensor is in contact with H_2 as a reducing agent, the electrons transfer from hydrogen into the Dy_{4f} orbitals and thus to oxygen,

creating superoxide anion radicals [50]. Therefore, the formation of highly reactive oxidant species including °OH, HO_2° and O_2°$^-$ on the Dy_2O_3-Pd-PDA/rGO heterojunction surface results in shaping the electron-hole pairs where the excited electrons from the valence band move to the conduction band and consequently leaving holes in the valence band [51]. These photoproduced electron-hole pairs can transfer to the surface, inducing the electron acceptor (O_2) to active oxygen ($^\circ O_2^-$) reduction process [52]. In addition, the holes oxidize H_2 (the electron donor) to produce hydroxyl radicals and/or H_2O molecules [52]. The active $^\circ O_2^-$ and OH° accelerate the oxidisation of the adsorbed H_2 molecules, enhancing the sensing performance [52]. Response magnitude of the sensor at 150 °C and 0 %RH was calculated for each experiment towards H_2 with different concentrations (200–600 ppm) in the dark and under UV radiation and presented in Table 1.

Table 1. Hydrogen sensing response of Dy_2O_3-Pd-PDA/rGO conductometric sensor in the dark and under UV illumination at 150 °C and 0 %RH towards H_2 with different concentrations.

		H_2 Concentration (ppm)				
		200	**300**	**400**	**500**	**600**
Response (%)	**In the dark**	100.3	100.68	100.72	100.75	100.75
	Under UV	100.7	101.3	102.2	103.1	104

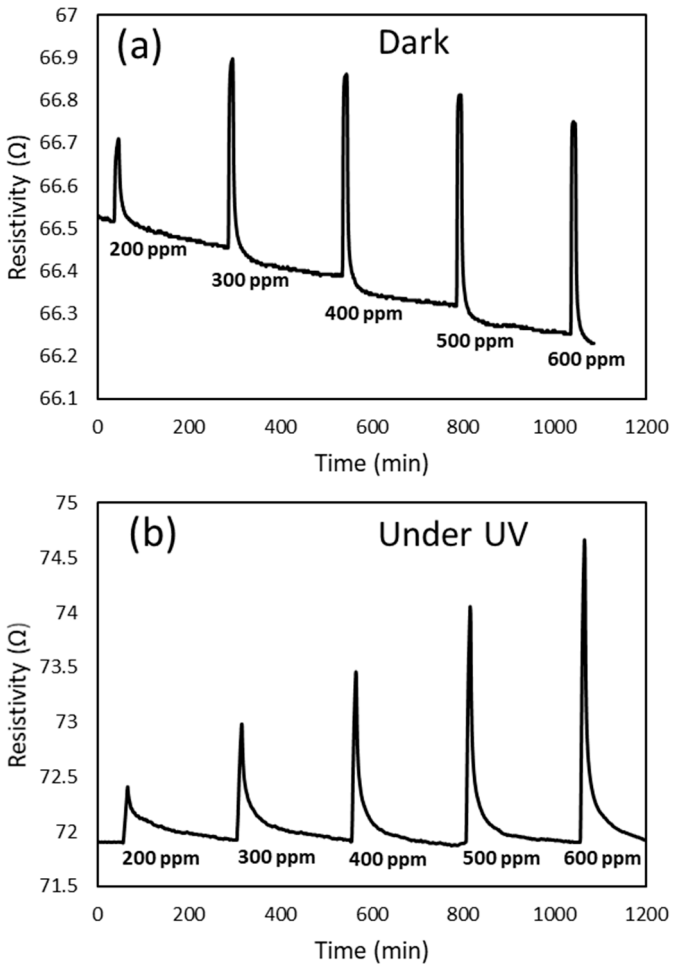

Figure 9. Dynamic response of Dy_2O_3-Pd-PDA/rGO sensor at 150 °C and 0 %RH as a function of hydrogen concentration, (**a**) without and (**b**) with UV illumination.

Table 1 confirms an improvement in the response of the photo-induced sensor under UV illumination because of the decrease in the adsorption energy barrier between the gas

molecules and sensing film [53]. In addition, the sensor's response in the dark is nearly constant by rising the H_2 concentration from 400 to 600 ppm, which can be attributed to the competition between recombination of the electron-hole pairs and the re-adsorption of the H_2 molecules [54,55]. The H_2 sensing mechanism of the Dy_2O_3-Pd-PDA/rGO nanocomposite-based sensor is complex and cannot be simplified based on different physical and chemical adsorption/desorption interactions, including van der Waals forces, π-π interactions, formation of various chemical bonds, oxygen species on the surface, and charge transfer between the heterojunction nanocomposite and H_2 molecules [56].

3.2.3. Effect of Relative Humidity

Some environmental elements can influence the gas sensing performance, including humidity [57]. In a humid environment, water molecules could adsorb onto the sensor as well, thus affecting the physisorption and chemisorption processes of hydrogen [48,58]. In this work, we investigated the effect of humidity (from 0 %RH to 25 %RH) on the Dy_2O_3-Pd-PDA/rGO sensor's performance at the optimum temperature of 150 °C under different H_2 concentrations and UV radiation.

The sensing parameters, including the response magnitude and response and recovery times towards H_2 with different concentrations and various %RH, was calculated for each experiment and presented in Tables 2 and 3. The results reveal that the sensor's responses to H_2 are enhanced by increasing the H_2 concentration from 200 ppm to 600 ppm. Table 2 also indicates that the sensor's responses are improved by elevating the %RH up to 15% and then is reduced by further increasing to 25%. In addition, it was seen that the electrical properties of the sensor remained almost constant by further raising the %RH above 25% up to 47.5%. The sensitivity improvement of up to 15 %RH can be attributed to the role of water molecules in humid environments, participating in physical and chemical adsorption/desorption reactions [59]. Similar to H_2, water molecules could also act as electron donors, so when the relative humidity elevates to 15%, the resistance of the p-type sensor rises, improving the sensor's response due to the increased number of adsorbed water molecules [59,60]. In addition, the polar hydroxyl and carbonyl functional groups present on the sensing material's surface can interact with water, causing a resistance change as well [61]. Therefore, the formation of the hydroxyl active sites on the surface of the Dy_2O_3-Pd-PDA/rGO due to the interaction between the adsorbed H_2 molecules and the present oxygen species on the sensing layer surface leads to improvement in the sensor's response [62]. By further increasing the relative humidity, the adsorbed water molecules concentration increases on the sensor's surface, breaking the sensing material's sublattice and symmetry (especially the graphene oxide) and continuously widening its bandgap, consequently changing the electrical properties of the sensor, and decreasing the sensor's response [63].

Table 2. Sensing parameters of the sensor towards 200–600 ppm H_2 at 150 °C under UV illumination at different humidity level.

H_2 Conc (ppm)	**Response (%)**				
	0 %RH	**10 %RH**	**15 %RH**	**20 %RH**	**25 %RH**
200	100.7	100.9	101.9	101.3	101.9
300	101.3	101.4	102.9	101.5	102.1
400	102.2	102.5	104.1	101.6	102.3
500	103.1	103.9	105.1	101.6	102.3
600	104	104.15	107.1	101.6	101.9

Table 3. Sensing parameters towards H_2 with 2000–6000 ppm concentrations at 150 °C under UV illumination.

H_2 Conc (ppm)	Response (%)			Response Time (s)			Recovery Time (s)		
	0 %RH	15 %RH	20 %RH	0 %RH	15 %RH	20 %RH	0 %RH	15 %RH	20 %RH
2000	104.3	114.12	113.5	60	600	720	180	240	180
3000	107.4	122.1	130.4	180	420	600	180	240	180
4000	111.6	131.9	142.6	180	420	360	180	240	120
5000	115.8	140.4	145.2	150	360	180	210	180	120
6000	121	144.1	144	150	300	180	240	180	120

In addition, excess water molecules on the sensing surface could compete with H_2 molecules to be adsorbed on the sensor's surface. Consequently, due to the larger molecule size of the water, it is challenging for them to compete with H_2 molecules to enter the sensing material's surface, resulting in a decrease in the sensing response [57].

The humidity effect was also investigated when the sensor was exposed to high H_2 concentrations from 2000 ppm to 6000 ppm. As shown in Table 3, the sensor demonstrates a maximum response of 121% at 0 %RH in the presence of 6000 ppm H_2 at 150 °C. By increasing the H_2 concentration, the number of hydrogen molecules interacting with the sensing layer rises, enhancing the adsorption rate on the surface until it gets saturated.

Table 3 also reveals that the sensor's responses enhance by raising the humidity to 20%. The sensor's response upon exposure to 6000 ppm H_2 at 20 %RH almost doubled. The response is calculated to be 144%, comparable with the sensor's response (144.1%) at 15 %RH under the same operational conditions. However, by increasing the H_2 concentration up to 5000 ppm at 20 %RH, the sensor's response slightly enhanced to 145.2% while it dropped a little by further growing the H_2 concentration to 6000 ppm. This can be attributed to the competition between the H_2 and water molecules to be adsorbed on the sensing layer's surface [46,64].

Another explanation can be seen in Figure 10, which shows the dynamic response of the sensor towards H_2 at 0 %RH, 15 %RH, and 20 %RH and 150 °C. Comparing these results reveals that a slight baseline drift occurs when the sensor is operating at 20 %RH, which means the sensor does not recover fully, decreasing the sensor's response while exposed to 6000 ppm H_2.

In addition, Figure 10a shows that the sensor's baseline (i.e., sensor's resistivity) at 0 %RH is higher than what it is at 15 %RH and 20 %RH. This result could be attributed to increasing the charge carriers on the surface of a sensing material by elevating the %RH due to the adsorbed ionised water molecules, enhancing the sensor's conductivity [61,64]. Moreover, the presence of hydroxyl active sites (as electron donors) on the sensing layer in the humid environment enhances the electric charge density by forming the hydronium cations from the ionised water molecules (Equation (4)), leading to an increase in the conductivity [48,58].

$$2H_2O \rightleftarrows OH^- + H_3O^{+\cdot} \quad (4)$$

Figure 10 also compares the response and recovery times while increasing the humidity level and H_2 concentrations. A fast response and recovery, 60 s and 180 s, respectively, were measured for 2000 ppm H_2 at 150 °C and 0 %RH. It can be seen that both response and recovery times decrease by rising the H_2 concentration at a higher humidity level than 0 %RH due to an increase in the surface coverage rate accelerating the adsorption/desorption of the H_2 molecules [65]. In addition, the high permeability of the Dy_2O_3-Pd-PDA/rGO to water molecules and the hoping proton mechanism play essential roles in the sensing performance [49,66]. When the concentration of the adsorbed water molecules increases on the surface (by increasing the %RH from 15% to 20%), the arisen protons (H^+), from hydroxyl functional groups of the rGO, bond with the water molecules. This leads to forming the hydronium ions, which enhance the electric charge density [39,63]. Thus, by increasing the concentration of the H_2 molecules, the adsorption/desorption interactions

become quicker due to the increased gas diffusion and conductive routes with high mobility [67,68]. Consequently, by comparing the response and recovery times at 15% and 20 %RH, we observe quicker response and recovery by increasing the H_2 concentration at 20 %RH. Moreover, by raising the humidity to 20%, the sensor's recovery became faster than it was at 0 % RH due to the physical and chemical adsorption/desorption rate of the H_2 molecules.

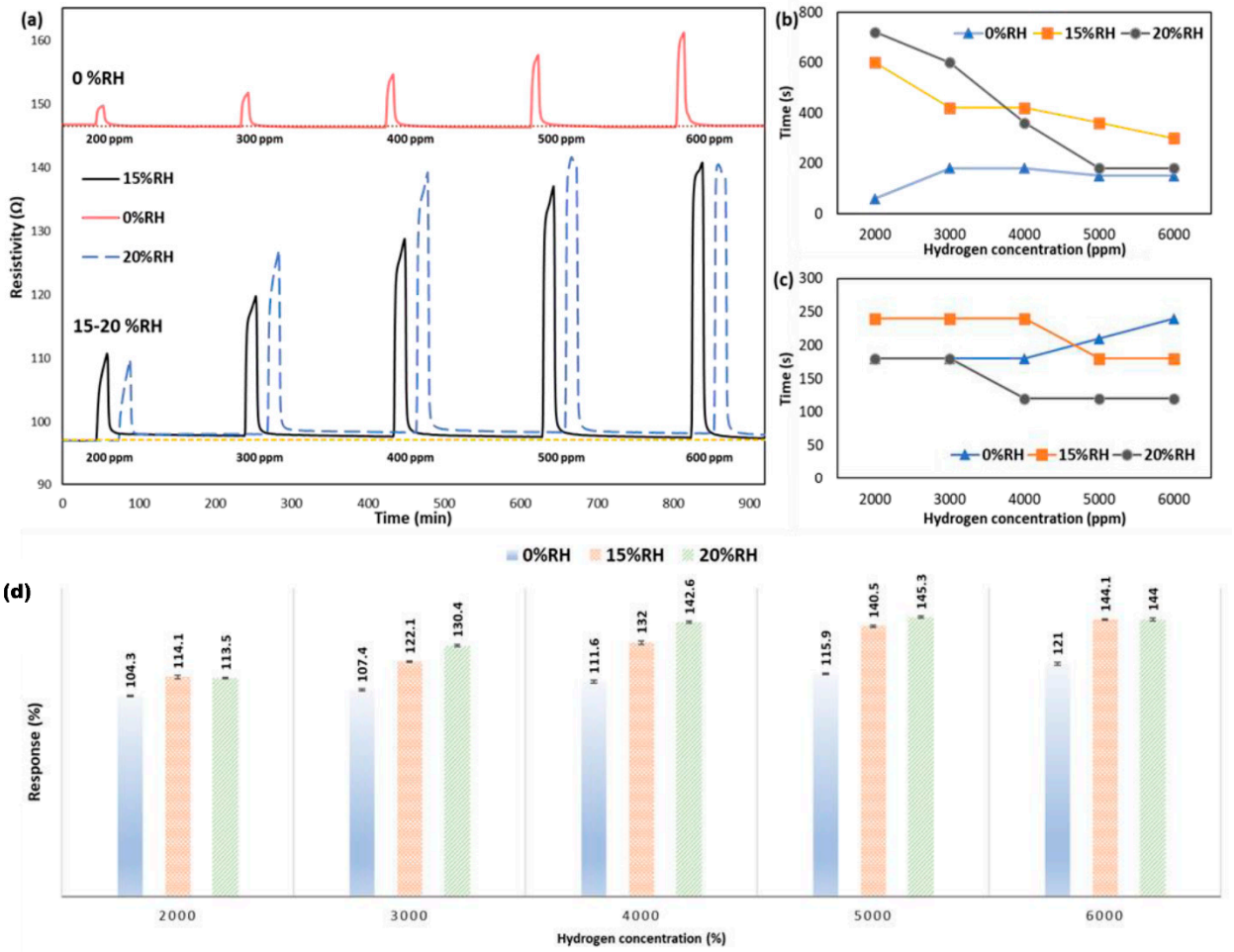

Figure 10. (**a**) Dynamic response of Dy_2O_3-Pd-PDA/rGO sensor towards H_2 with different concentrations (2000–6000 ppm) at 150 °C, and relative humidity levels (0 %RH, 15 %RH, and 20 %RH) under UV radiation; (**b**) response time and (**c**) recovery time of the sensor at 0 %RH, 15 %RH, and 20 %RH as a function of H_2 concentrations. (**d**) Response magnitude of the sensor towards H_2 with different concentrations at 0 %RH, 15 %RH, and 20 %RH.

A fast recovery (120 s) was measured for 4000 to 6000 ppm H_2 at 150 °C and 20 %RH. In a humid environment, it was observed that the response and recovery were quicker by increasing the H_2 concentration based on an increase in the surface coverage rate facilitating the adsorption/desorption of the H_2 molecules. In addition, the sensor saturates faster at higher concentrations. Moreover, the functional groups on the Dy_2O_3-Pd-PDA/rGO, including the hydroxyl and carbonyl groups, can interact with water, changing the adsorption/desorption rate and participating in the physisorption of the H_2 molecules on the Dy_2O_3-Pd-PDA/rGO surface, based on Van der Waals forces, and also forming the covalent bonds via the chemisorption reactions [65]. The water molecules usually behave as electron donors, inducing the ionisation of the OH and COOH functional groups in the sensing layer to generate a concentration gradient of protons [13]. This gradient accelerates the diffusion of the protons to the sensing material, delivering a voltage and current in

the external circuit that leads to a quicker response [69]. Figure 10d shows the response percentage of the sensor at 0 %RH, 15 %RH, and 20 %RH and 150 °C. The highest response is calculated to be 145.2% when the sensor is exposed to 5000 ppm H_2 at 20 %RH.

3.2.4. Sensor Selectivity and Long-Term Stability

The gas selectivity of the Dy_2O_3-Pd-PDA/rGO sensor was investigated at the optimum temperature of 150 °C and 0 %RH. Figure 11a shows the response of the sensor to 50 ppm H_2 gas as compared with different interfering gases (all at 50 ppm concentrations), including methane (CH_4), ammonia (NH_3), and acetone (C_3H_6O). The sensor indicated a remarkable response of 100.5% towards hydrogen while showing a negligible response (2.1%) towards acetone and inadequate responses of 5.1% and 3.2% towards CH_4 and NH_3, respectively. As mentioned before, the sensing mechanism of the p-type Dy_2O_3-Pd-PDA/rGO nanocomposite is mainly based on the chemical adsorption/desorption interactions of the oxygen active sites with the H_2 molecules and the charge transfer from the H_2 molecules to the sensing layer [24,70]. The oxygen in the air interacts with the free electrons on the sensing layer surface, forming O^{2-}, O_2^-, and O^- ions. These reactive oxygen species interact with the H_2 molecules as an electron donor gas, enhancing the electron charge transfer to the sensing layer, reducing the hole concentration, and increasing resistivity [24,41,42]. The Dy_2O_3-Pd-PDA/rGO sensor was examined repeatedly over eight months towards 6000 ppm H_2 at 150 °C and 0 %RH and indicated long term stability with a negligible degradation (Figure 11b).

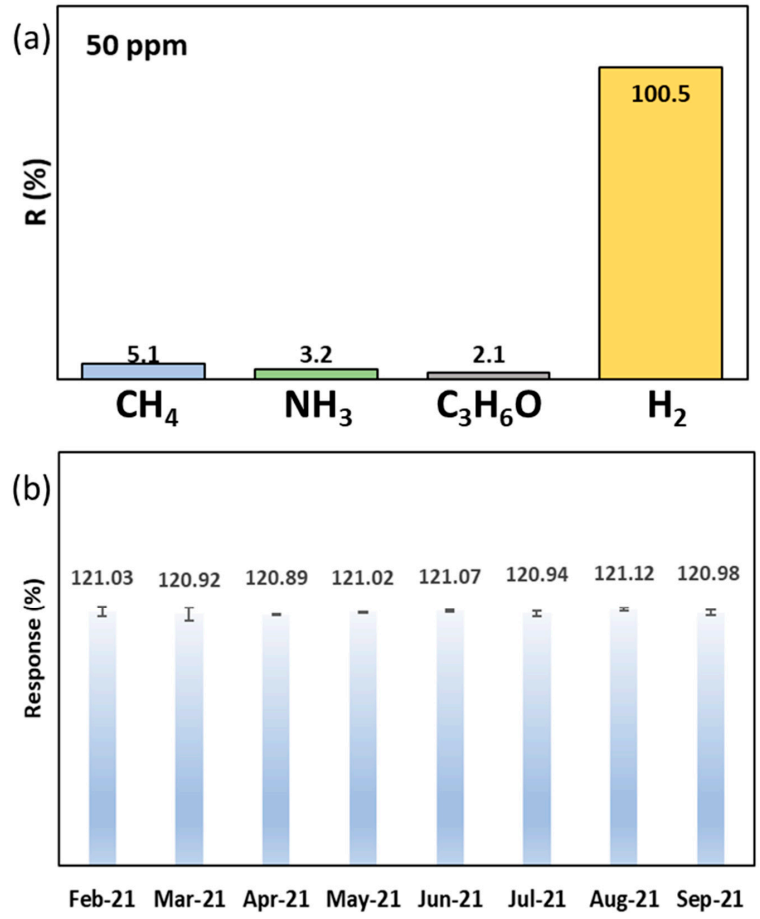

Figure 11. (**a**) Gas selectivity of the Dy_2O_3-Pd-PDA/rGO sensor towards 50 ppm of different gases, (**b**) long term stability of the sensor's response towards 6000 ppm H_2 at 150 °C and 0 %RH over eight months.

4. Discussion and Conclusions

The heterojunction Dy_2O_3-Pd-PDA/rGO nanocomposite was synthesised by an environmentally friendly and straightforward chemical procedure [22]. The surface characteristics of the sensor revealed a uniform distribution of 2D Dy_2O_3 and Pd NPs onto the PDA/rGO nanosheets. The SEM images illustrated a multi-layered porous structure of the Dy_2O_3-Pd-PDA/rGO nanocomposite that considerably impacted the H_2 gas sensing performance. Raman analysis showed no significant defects in Pd-PDA/rGO NSs while doping with 2D Dy_2O_3. The hydrogen gas sensing performance of the fabricated conductometric sensor was extensively studied under different operational conditions, including H_2 concentration (50–6000 ppm), temperature (up to 200 °C), UV radiation, and relative humidity (up to 25 %RH). The sensor showed a negligible response to hydrogen without UV illumination. In contrast, the response was enhanced significantly under UV illumination due to stimulated electrons from the valence band of the sensing material [47]. These photogenerated electrons accelerate the adsorption and desorption reactions of H_2 molecules with the ambient oxygen species or water molecules [47].

The experimental results confirmed a p-type sensing behaviour with a maximum response of 121% towards 6000 ppm H_2 at 0 %RH and an optimum working temperature of 150 °C. This result could be attributed to increasing the concentration of the H_2 molecules, facilitating their interactions with the sensing material. Thus, enhancing the adsorption/desorption rate on the surface until it saturates and a steady state is reached. The sensor was capable of detecting the H_2 concentration as low as 50 ppm (R = 100.5%).

Gas sensing performance is correlated with the adsorption of atmospheric H_2O molecules as a significant source of interference [9,18]. Based on the literature, humidity is a complex challenge faced by most resistive H_2 sensors [9,71,72]. Therefore, developing a sensor capable of detecting H_2 in a humid environment can be a critical solution for humidity-related issues in the real environment [73]. Hence, we studied the effect of humidity on the Dy_2O_3-Pd-PDA/rGO nanocomposite sensing performance and its behaviour on the adsorption/desorption of H_2 molecules as one of the critical factors of developing a commercial sensor for humid environments [74]. It was observed that by increasing the %RH up to 20%, the sensor's performance (i.e., response and recovery times) drastically improved so that its response towards 5000 ppm H_2 at 150 °C was changed from 115.8% at 0 %RH to 145.2% at 20 %RH.

In addition, a maximum response of 144% was obtained upon exposure to 6000 ppm H_2 at 20 %RH and 150 °C, which is much higher than its response in a dry ambient (121%) at similar operational conditions. This result could be due to rising the charge carriers on the sensing layer surface by enriching the %RH because of the adsorbed ionised water molecules, in addition to the presence of the electron donor hydroxyl active sites on the sensing layer in the humid environment. By raising the %RH (from 15% to 20%), the sensor's response and recovery times also improved from 360 s to 180 s and 180 s to 120 s, respectively. Table 4 summarises a comparison of H_2 sensing performance between selected graphene-based nanomaterials, which are functionalised by noble metals and/or metal oxides with the current work.

In this work, reducing the GO by adding the DA, as an environmentally friendly chemical, highly improved its reduction process and functionalising the PDA/rGO with Pd NPs and 2D Dy_2O_3 significantly enhanced the H_2 sensing parameters [19]. In addition, the developed Dy_2O_3-Pd-PDA/rGO sensor was highly selective to hydrogen and illustrated high effectiveness in the humid environment.

Table 4. H_2 sensing properties of different graphene-based materials functionalised by noble metals and/or metal oxides.

Material.	Synthesis Method	Hybrid Material	Temp. (°C)	RH (%)	H_2 Conc. (ppm)	Response Time (s)	Recovery Time (s)	Response (%)
Graphene [75]	Thermal CVD	Pd NPs-SiO_2	RT	-	500	213	600	4.1
rGO [76]	Freeze drying	NiO	50	-	10,000	28	142	0.64
rGO [8]	Wet chemistry	Pd NPs	100	10	5000	170	1440	18.2
rGO [77]	Hummers' method, Hydrothermal	Pd-Pt	25	-	8000	300	600	0.52
rGO [78]	Hummers' method, Hydrothermal	Pt-SnO_2	RT	-	5000	3	2	3
PDA/rGO (this work)	Wet chemistry	Pd NPs-2D Dy_2O_3	150	20	5000	180	120	145.2

According to the literature, the hybrid materials' sensing performance can be enhanced by surface engineering due to forming the new physical and electrical properties, including the changes in thickness and several reactive sites for gas molecules interactions [79,80]. Overall, these enhancements could be based on improved electrical properties and charge transfer of the hybrid sensing material [81]. However, the hybrid materials gas sensing mechanisms seem to be complex, so to achieve predictable sensing improvements, many variants need to be investigated, such as the impact of different fabrication techniques, functionalisation, and structural parameters such as the porosity, thickness, surface to volume ratio and crystallinity of the materials. The mentioned parameters play critical roles in the sensing material and gas interactions, consequently changing the sensing performance [82]. However, these effects on the chemical and electrical properties of the sensors and thus enhancement in gas sensing properties may not be directly related.

In this work, the presence of oxygen species (O_2^-, O^-, and O^{2-}) on the sensing material surface under UV illumination played a critical role in the molecular adsorption of the fabricated p-type gas sensors, forming the photo-induced electron-hole pairs and an electron depleted region [15,83]. When the Dy_2O_3-Pd-PDA/rGO heterojunction nanocomposite is exposed to hydrogen as a reducing gas, the reduction reaction between the oxygen species and H_2 molecules accrue on the Dy_2O_3 surface, creating the Dy^{3+} due to the oxygen vacancy. This results in releasing the electron to the sensing layer's surface, affecting the depletion layer and resistance of the sensor [24]. At the same time, hybridising the Dy_2O_3 with Pd-PDA/rGO formed a p-n junction nanocomposite, creating Dy-O bondings at the interface between Dy_2O_3 and rGO, which positively affected the H_2 sensing performance of the final nanocomposite at a low operating temperature [84,85]. Another benefit of hybridisation was the formation of Pd-O-Dy bonds as active sites in the interface between the Dy_2O_3 and Pd NPs, facilitating the chemisorption of the H_2 molecules with the lattice oxygen, which also creates a synergic effect on the durability of the material due to anchoring the Pd NPs with the active sites' support [85].

To conclude, the results confirmed the regulated electronic structure of the Dy_2O_3-Pd-PDA/rGO heterojunction nanocomposite at the interface region, resulting in reduced energy barrier, enhanced kinetics, and more balanced hydrogen adsorption/desorption rate [86]. Moreover, the experimentally determined performance of the Dy_2O_3-Pd-PDA/rGO heterojunction nanocomposite revealed to be reliable, sensitive, have a rapid response, and recovery sensing materials, which has benefited from the use of environmentally friendly and simple synthesis and fabrication techniques as well as improvements in the combinations of Pd NPs and 2D Dy_2O_3 that comprise the composite sensor.

Author Contributions: H.H.: Conceptualisation, methodology, investigation, software, sensor devices fabrications, material characterisations, gas sensing data collection, data analysis, data interpretation and validation, data visualisation, writing—original and final draft preparation. A.Y.: material synthesis, review and editing the draft. S.J.: supervision, review and editing the draft. M.S.: main supervision, review and editing the draft, funding acquisition, resources. All authors have read and agreed to the published version of the manuscript.

Funding: This research was funded by the Australian Renewable Energy Agency (ARENA) as part of ARENA's Research and Development Program—Renewable Hydrogen for Export (Contract No. 2018/RND012). This research was supported by using the Nectar Research Cloud, a collaborative Australian research platform supported by the NCRIS-funded Australian Research Data Commons (ARDC).

Data Availability Statement: Not applicable.

Acknowledgments: This research was funded by the Australian Renewable Energy Agency (ARENA) as part of ARENA's Research and Development Program—Renewable Hydrogen for Export (Contract No. 2018/RND012). The views expressed herein are not necessarily the views of the Australian Government, and the Australian Government does not accept responsibility for any information or advice contained herein. We would like to acknowledge Christopher Harrison and Andrew Moore for their support in developing the gas sensing system at Swinburne. This research was supported by using the Nectar Research Cloud, a collaborative Australian research platform supported by the NCRIS-funded Australian Research Data Commons (ARDC). The authors would like to thank Jamie Riches for assistance in obtaining TEM images at the Central Analytical Research Facility at QUT.

Conflicts of Interest: The authors declare no conflict of interest.

References

1. Hashtroudi, H.; Atkin, P.; Mackinnon, I.D.R.; Shafiei, M. Low-operating temperature resistive nanostructured hydrogen sensors. *Int. J. Hydrogen Energy* **2019**, *44*, 26646–26664. [CrossRef]
2. Buttner, W.J.; Post, M.B.; Burgess, R.; Rivkin, C. An overview of hydrogen safety sensors and requirements. *Int. J. Hydrogen Energy* **2011**, *36*, 2462–2470. [CrossRef]
3. Hübert, T.; Boon-Brett, L.; Black, G.; Banach, U. Hydrogen sensors—A review. *Sens. Actuators B Chem.* **2011**, *157*, 329–352. [CrossRef]
4. Li, B.L.; Wang, J.; Zou, H.L.; Garaj, S.; Lim, C.T.; Xie, J.; Li, N.B.; Leong, D. Low-Dimensional Transition Metal Dichalcogenide Nanostructures Based Sensors. *Adv. Funct. Mater.* **2016**, *26*, 7034–7056. [CrossRef]
5. Ilnicka, A.; Lukaszewicz, J.P. Graphene-Based Hydrogen Gas Sensors: A Review. *Processes* **2020**, *8*, 633. [CrossRef]
6. Pham, T.K.N.; Brown, J.J. Hydrogen Sensors Using 2-Dimensional Materials: A Review. *ChemistrySelect* **2020**, *5*, 7277–7297. [CrossRef]
7. Weng, Q.; Li, G.; Feng, X.; Nielsch, K.; Golberg, D.; Schmidt, O.G. Electronic and Optical Properties of 2D Materials Constructed from Light Atoms. *Adv. Mater.* **2018**, *30*, e1801600. [CrossRef]
8. Hashtroudi, H.; Kumar, R.; Savu, R.; Moshkalev, S.; Kawamura, G.; Matsuda, A.; Shafiei, M. Hydrogen gas sensing properties of microwave-assisted 2D Hybrid Pd/rGO: Effect of temperature, humidity and UV illumination. *Int. J. Hydrogen Energy* **2021**, *46*, 7653–7665. [CrossRef]
9. Joshi, N.; Hayasaka, T.; Liu, Y.; Liu, H.; Oliveira, O.N., Jr.; Lin, L.J.M.A. A review on chemiresistive room temperature gas sensors based on metal oxide nanostructures, graphene and 2D transition metal dichalcogenides. *Microchim. Acta* **2018**, *185*, 213. [CrossRef] [PubMed]
10. Fang, W.; Yang, Y.; Yu, H.; Dong, X.; Wang, R.; Wang, T.; Wang, J.; Liu, Z.; Zhao, B.; Wang, X. An In_2O_3 nanorod-decorated reduced graphene oxide composite as a high-response NOx gas sensor at room temperature. *New J. Chem.* **2017**, *41*, 7517–7523. [CrossRef]
11. Varghese, S.S.; Varghese, S.H.; Swaminathan, S.; Singh, K.K.; Mittal, V. Two-Dimensional Materials for Sensing: Graphene and Beyond. *Electronics* **2015**, *4*, 651–687. [CrossRef]
12. Shi, J.; Cheng, Z.; Gao, L.; Zhang, Y.; Xu, J.; Zhao, H. Facile synthesis of reduced graphene oxide/hexagonal WO3 nanosheets composites with enhanced H_2S sensing properties. *Sens. Actuators B Chem.* **2016**, *230*, 736–745. [CrossRef]
13. Luo, Y.; Zhang, C.; Zheng, B.; Geng, X.; Debliquy, M. Hydrogen sensors based on noble metal doped metal-oxide semiconductor: A review. *Int. J. Hydrogen Energy* **2017**, *42*, 20386–20397. [CrossRef]
14. Anand, K.; Singh, O.; Singh, M.P.; Kaur, J.; Singh, R.C. Hydrogen sensor based on graphene/ZnO nanocomposite. *Sens. Actuators B Chem.* **2014**, *195*, 409–415. [CrossRef]
15. Boudiba, A.; Roussel, P.; Zhang, C.; Olivier, M.-G.; Snyders, R.; Debliquy, M. Sensing mechanism of hydrogen sensors based on palladium-loaded tungsten oxide (Pd–WO3). *Sens. Actuators B Chem.* **2013**, *187*, 84–93. [CrossRef]
16. Novoselov, K. Nobel Lecture: Graphene: Materials in the Flatland. *Rev. Mod. Phys.* **2011**, *83*, 837–849. [CrossRef]
17. Armgarth, M.; Söderberg, D.; Lundström, I. Palladium and platinum gate metal-oxide-semiconductor capacitors in hydrogen and oxygen mixtures. *Appl. Phys. Lett.* **1982**, *41*, 654–655. [CrossRef]
18. Bindra, P.; Hazra, A. Capacitive gas and vapor sensors using nanomaterials. *J. Mater. Sci. Mater. Electron.* **2018**, *29*, 6129–6148. [CrossRef]
19. Johnson, J.L.; Behnam, A.; Pearton, S.; Ural, A. Hydrogen Sensing Using Pd-Functionalized Multi-Layer Graphene Nanoribbon Networks. *Adv. Mater.* **2010**, *22*, 4877–4880. [CrossRef]

20. Silva, C.; Simon, F.; Friedel, P.; Pötschke, P.; Zimmerer, C. Elucidating the Chemistry behind the Reduction of Graphene Oxide Using a Green Approach with Polydopamine. *Nanomaterials* **2019**, *9*, 902. [CrossRef]
21. Xu, L.Q.; Yang, W.J.; Neoh, K.-G.; Kang, E.-T.; Fu, G.D. Dopamine-Induced Reduction and Functionalization of Graphene Oxide Nanosheets. *Macromolecules* **2010**, *43*, 8336–8339. [CrossRef]
22. Fu, L.; Lai, G.; Zhu, D.; Jia, B.; Malherbe, F.; Yu, A. Advanced Catalytic and Electrocatalytic Performances of Polydopamine-Functionalized Reduced Graphene Oxide-Palladium Nanocomposites. *ChemCatChem* **2016**, *8*, 2975–2980. [CrossRef]
23. Su, Y.-D.; Shih, W.-C.; Lee, J.Y.-M. The characterization of retention properties of metal–ferroelectric ($PbZr_{0.53}Ti_{0.47}$ $47O_3$)–insulator (Dy_2O_3, Y_2O_3)–semiconductor devices. *Microelectron. Reliab.* **2007**, *47*, 619–622. [CrossRef]
24. Dong, X.; Cheng, X.; Zhang, X.; Sui, L.; Xu, Y.; Gao, S.; Zhao, H.; Huo, L. A novel coral-shaped Dy_2O_3 gas sensor for high sensitivity NH3 detection at room temperature. *Sens. Actuators B Chem.* **2017**, *255*, 1308–1315. [CrossRef]
25. Pan, T.-M.; Lin, C.-W. Structural and Sensing Characteristics of Dy_2O_3 and Dy_2TiO_5 Electrolyte−Insulator−Semiconductor pH Sensors. *J. Phys. Chem. C* **2010**, *114*, 17914–17919. [CrossRef]
26. Nur-E-Alam, M.; Vasiliev, M.; Kotov, V.; Alameh, K. Recent Developments in Magneto-optic Garnet-type Thin-film Materials Synthesis. *Procedia Eng.* **2014**, *76*, 61–73. [CrossRef]
27. Vuong, Q.L.; Van Doorslaer, S.; Bridot, J.-L.; Argante, C.; Alejandro, G.; Hermann, R.; Disch, S.; Mattea, C.; Stapf, S.; Gossuin, Y. Paramagnetic nanoparticles as potential MRI contrast agents: Characterization, NMR relaxation, simulations and theory. *Magn. Reson. Mater. Phys. Biol. Med.* **2012**, *25*, 467–478. [CrossRef]
28. He, B.; Zhao, L.; Wang, W.; Chen, F.; Xia, C. Electro-catalytic activity of Dy_2O_3 as a solid oxide fuel cell anode material. *Electrochem. Commun.* **2011**, *13*, 194–196. [CrossRef]
29. Andrade, E.N.D.C.; Lonsdale, K.Y. *William Henry Bragg, 1862–1942*; Royal Society Publishing: London, UK, 1943.
30. Klung, H.; Alexander, L. *X-ray Diffraction Procedures*; John Wiley & Sons: New York, NY, USA, 1962; Volume 1, p. 974.
31. Sharma, N.D.; Singh, J.; Dogra, S.; Varandani, D.; Poswal, H.K.; Sharma, S.M.; Bandyopadhyay, A.K. Pressure-induced anomalous phase transformation in nano-crystalline dysprosium sesquioxide. *J. Raman Spectrosc.* **2011**, *42*, 438–444. [CrossRef]
32. Verma, R.; Samdarshi, S.K. In Situ Decorated Optimized CeO_2 on Reduced Graphene Oxide with Enhanced Adsorptivity and Visible Light Photocatalytic Stability and Reusability. *J. Phys. Chem. C* **2016**, *120*, 22281–22290. [CrossRef]
33. Anema, J.R.; Li, J.-F.; Yang, Z.-L.; Ren, B.; Tian, Z.-Q. Shell-Isolated Nanoparticle-Enhanced Raman Spectroscopy: Expanding the Versatility of Surface-Enhanced Raman Scattering. *Annu. Rev. Anal. Chem.* **2011**, *4*, 129–150. [CrossRef]
34. Liu, Y.; Wang, F.; Liu, Y.; Wang, X.; Xu, Y.; Zhang, R. Charge transfer at carbon nanotube–graphene van der Waals heterojunctions. *Nanoscale* **2016**, *8*, 12883–12886. [CrossRef]
35. Zhang, B.; Cheng, M.; Liu, G.; Gao, Y.; Zhao, L.; Li, S.; Wang, Y.; Liu, F.; Liang, X.; Zhang, T.; et al. Room temperature NO_2 gas sensor based on porous Co_3O_4 slices/reduced graphene oxide hybrid. *Sens. Actuators B Chem.* **2018**, *263*, 387–399. [CrossRef]
36. Shen, Y.; Lu, S.; Xu, W.; Lv, A.; Wang, Z.; Wang, H.; Liu, G.; Zhang, Y. Fabrication of Composite Material with Pd Nanoparticles and Graphene on Nickel Foam for Its Excellent Electrocatalytic Performance. *Electrocatalysis* **2020**, *11*, 522–535. [CrossRef]
37. Eifert, B.; Becker, M.; Reindl, C.T.; Giar, M.; Zheng, L.; Polity, A.; He, Y.; Heiliger, C.; Klar, P.J. Raman studies of the intermediate tin-oxide phase. *Phys. Rev. Mater.* **2017**, *1*, 014602. [CrossRef]
38. Dresselhaus, M.S.; Jorio, A.; Filho, A.G.S.; Saito, R. Defect characterization in graphene and carbon nanotubes using Raman spectroscopy. *Philos. Trans. R. Soc. London. Ser. A Math. Phys. Eng. Sci.* **2010**, *368*, 5355–5377. [CrossRef] [PubMed]
39. Hashtroudi, H.; Mackinnon, I.D.R.; Shafiei, M. Emerging 2D hybrid nanomaterials: Towards enhanced sensitive and selective conductometric gas sensors at room temperature. *J. Mater. Chem. C* **2020**, *8*, 13108–13126. [CrossRef]
40. Kapoor, A.; Ritter, J.A.; Yang, R.T. An extended Langmuir model for adsorption of gas mixtures on heterogeneous surfaces. *Langmuir* **1990**, *6*, 660–664. [CrossRef]
41. Voiry, D.; Yang, J.; Chhowalla, M. Recent Strategies for Improving the Catalytic Activity of 2D TMD Nanosheets Toward the Hydrogen Evolution Reaction. *Adv. Mater.* **2016**, *28*, 6197–6206. [CrossRef] [PubMed]
42. Sun, Y.-F.; Liu, S.-B.; Meng, F.-L.; Liu, J.-Y.; Jin, Z.; Kong, L.-T.; Liu, J.-H. Metal Oxide Nanostructures and Their Gas Sensing Properties: A Review. *Sensors* **2012**, *12*, 2610–2631. [CrossRef]
43. Rajkumar, K.; Kumar, R.R. Gas sensors based on two-dimensional materials and its mechanisms. In *Fundamentals and Sensing Applications of 2D Materials*; Elsevier: Amsterdam, The Netherlands, 2019; pp. 205–258.
44. Du, H.; Xie, G.; Su, Y.; Tai, H.; Du, X.; Yu, H.; Zhang, Q. A New Model and Its Application for the Dynamic Response of RGO Resistive Gas Sensor. *Sensors* **2019**, *19*, 889. [CrossRef] [PubMed]
45. Rout, C. *Fundamentals and Sensing Applications of 2D Materials*; Woodhead Publishing: Duxford, UK, 2019.
46. Potje-Kamloth, K. Semiconductor Junction Gas Sensors. *Chem. Rev.* **2008**, *108*, 367–399. [CrossRef] [PubMed]
47. Kumar, R.; Liu, X.; Zhang, J.; Kumar, M. Room-Temperature Gas Sensors Under Photoactivation: From Metal Oxides to 2D Materials. *Nano-Micro Lett.* **2020**, *12*, 164. [CrossRef] [PubMed]
48. Sharma, R.; Rawal, D. *The Physics of Semiconductor Devices: Proceedings of IWPSD 2017*; Springer: Berlin/Heidelberg, Germany, 2018; Volume 215.
49. Meng, Z.; Stolz, R.M.; Mendecki, L.; Mirica, K.A. Electrically-Transduced Chemical Sensors Based on Two-Dimensional Nanomaterials. *Chem. Rev.* **2019**, *119*, 478–598. [CrossRef] [PubMed]

50. Bellardita, M.; Fiorenza, R.; Palmisano, L.; Sciré, S. Photocatalytic and photo-thermo-catalytic applications of cerium oxide-based material. In *Cerium Oxide (CeO_2): Synthesis, Properties and Applications*; a Volume in Metal Oxides Series; Elsevier: Amsterdam, The Netherlands, 2020; ISBN 978-0-12-815661-2. [CrossRef]
51. Chen, X.; Shen, S.; Guo, L.; Mao, S.S. Semiconductor-based Photocatalytic Hydrogen Generation. *Chem. Rev.* **2010**, *110*, 6503–6570. [CrossRef]
52. Chen, X.; Mao, S.S. Titanium dioxide nanomaterials: Synthesis, properties, modifications, and applications. *Chem. Rev.* **2007**, *107*, 2891–2959. [CrossRef]
53. Muckley, E.S.; Nelson, A.J.; Jacobs, C.B.; Ivanov, I.N. Effect of UV irradiation on adsorption/desorption of oxygen and water on carbon nanotubes. *Org. Photonic Mater. Devices* **2016**, *9745*, 97451. [CrossRef]
54. Sun, P.; Zhu, M.; Wang, K.; Zhong, M.; Wei, J.; Wu, D.; Cheng, Y.; Zhu, H. Photoinduced molecular desorption from graphene films. *Appl. Phys. Lett.* **2012**, *101*, 53107. [CrossRef]
55. Azpiroz, J.M.; Ronca, E.; De Angelis, F. Photoinduced Energy Shift in Quantum-Dot-Sensitized TiO_2: A First-Principles Analysis. *J. Phys. Chem. Lett.* **2015**, *6*, 1423–1429. [CrossRef]
56. Chauhan, P.S.; Bhattacharya, S. Hydrogen gas sensing methods, materials, and approach to achieve parts per billion level detection: A review. *Int. J. Hydrogen Energy* **2019**, *44*, 26076–26099. [CrossRef]
57. Moon, J.; Cheng, Y.; Daemen, L.L.; Li, M.; Polo-Garzon, F.; Ramirez-Cuesta, A.J.; Wu, Z. Discriminating the Role of Surface Hydride and Hydroxyl for Acetylene Semihydrogenation over Ceria through In Situ Neutron and Infrared Spectroscopy. *ACS Catal.* **2020**, *10*, 5278–5287. [CrossRef]
58. Chen, Y.; Pei, Y.; Jiang, Z.; Shi, Z.; Xu, J.; Wu, D.; Xu, T.; Tian, Y.; Wang, X.; Li, X. Humidity sensing properties of the hydrothermally synthesized WS2-modified SnO_2 hybrid nanocomposite. *Appl. Surf. Sci.* **2018**, *447*, 325–330. [CrossRef]
59. Yavari, F.; Koratkar, N. Graphene-Based Chemical Sensors. *J. Phys. Chem. Lett.* **2012**, *3*, 1746–1753. [CrossRef]
60. Dimiev, A.M.; Alemany, L.B.; Tour, J.M. Graphene Oxide. Origin of Acidity, Its Instability in Water, and a New Dynamic Structural Model. *ACS Nano* **2012**, *7*, 576–588. [CrossRef]
61. Yan, W.; Worsley, M.A.; Pham, T.; Zettl, A.; Carraro, C.; Maboudian, R. Effects of ambient humidity and temperature on the NO2 sensing characteristics of WS2/graphene aerogel. *Appl. Surf. Sci.* **2018**, *450*, 372–379. [CrossRef]
62. Inpaeng, S.; Muangrat, W.; Tedsree, K.; Pfeiler, W.; Chodjarusawad, T.; Issro, C. Effective hydrogen gas sensor based on palladium nanoparticles dispersed on graphene sheets by spin coating technique. *Mater. Sci.* **2020**, *38*, 305–311. [CrossRef]
63. Yao, Y.; Chen, X.; Zhu, J.; Zeng, B.; Wu, Z.; Li, X. The effect of ambient humidity on the electrical properties of graphene oxide films. *Nanoscale Res. Lett.* **2012**, *7*, 363. [CrossRef]
64. Piloto, C.; Shafiei, M.; Khan, H.; Gupta, B.; Tesfamichael, T.; Motta, N. Sensing performance of reduced graphene oxide-Fe doped WO_3 hybrids to NO_2 and humidity at room temperature. *Appl. Surf. Sci.* **2018**, *434*, 126–133. [CrossRef]
65. Buscema, M.; Island, J.O.; Groenendijk, D.J.; Blanter, S.I.; Steele, G.A.; van der Zant, H.S.J.; Castellanos-Gomez, A. Photocurrent generation with two-dimensional van der Waals semiconductors. *Chem. Soc. Rev.* **2015**, *44*, 3691–3718. [CrossRef]
66. Nair, R.R.; Wu, H.A.; Jayaram, P.N.; Grigorieva, I.V.; Geim, A.K. Unimpeded Permeation of Water Through Helium-Leak-Tight Graphene-Based Membranes. *Science* **2012**, *335*, 442–444. [CrossRef]
67. Toda, K.; Furue, R.; Hayami, S. Recent progress in applications of graphene oxide for gas sensing: A review. *Anal. Chim. Acta* **2015**, *878*, 43–53. [CrossRef] [PubMed]
68. Esfandiar, A.; Ghasemi, S.; Zad, A.I.; Akhavan, O.; Gholami, M. The decoration of TiO_2/reduced graphene oxide by Pd and Pt nanoparticles for hydrogen gas sensing. *Int. J. Hydrogen Energy* **2012**, *37*, 15423–15432. [CrossRef]
69. Borini, S.; White, R.; Wei, D.; Astley, M.; Haque, S.; Spigone, E.; Harris, N.; Kivioja, J.; Ryhänen, T. Ultrafast Graphene Oxide Humidity Sensors. *ACS Nano* **2013**, *7*, 11166–11173. [CrossRef] [PubMed]
70. Seiyama, T.; Kato, A.; Fujiishi, K.; Nagatani, M. A New Detector for Gaseous Components Using Semiconductive Thin Films. *Anal. Chem.* **1962**, *34*, 1502–1503. [CrossRef]
71. Hassan, K.; Chung, G.-S. Catalytically activated quantum-size Pt/Pd bimetallic core–shell nanoparticles decorated on ZnO nanorod clusters for accelerated hydrogen gas detection. *Sens. Actuators B Chem.* **2017**, *239*, 824–833. [CrossRef]
72. Zhang, J.; Liu, X.; Neri, G.; Pinna, N. Nanostructured Materials for Room-Temperature Gas Sensors. *Adv. Mater.* **2015**, *28*, 795–831. [CrossRef]
73. Chatterjee, S.G.; Chatterjee, S.; Ray, A.K.; Chakraborty, A.K. Graphene–metal oxide nanohybrids for toxic gas sensor: A review. *Sens. Actuators B Chem.* **2015**, *221*, 1170–1181. [CrossRef]
74. Tripathi, K.; Kim, T.; Losic, D.; Tung, T.T. Recent advances in engineered graphene and composites for detection of volatile organic compounds (VOCs) and non-invasive diseases diagnosis. *Carbon* **2016**, *110*, 97–129. [CrossRef]
75. Wu, W.; Liu, Z.; Jauregui, L.A.; Yu, Q.; Pillai, R.; Cao, H.; Bao, J.; Chen, Y.P.; Pei, S.-S. Wafer-scale synthesis of graphene by chemical vapor deposition and its application in hydrogen sensing. *Sens. Actuators B Chem.* **2010**, *150*, 296–300. [CrossRef]
76. Ren, H.; Gu, C.; Joo, S.W.; Zhao, J.; Sun, Y.; Huang, J. Effective hydrogen gas sensor based on NiO@rGO nanocomposite. *Sens. Actuators B Chem.* **2018**, *266*, 506–513. [CrossRef]
77. Peng, Y.; Ye, J.; Zheng, L.; Zou, K. The hydrogen sensing properties of Pt–Pd/reduced graphene oxide based sensor under different operating conditions. *RSC Adv.* **2016**, *6*, 24880–24888. [CrossRef]

78. Russo, P.; Donato, N.; Leonardi, S.G.; Baek, S.; Conte, D.E.; Neri, G.; Pinna, N. Room-Temperature Hydrogen Sensing with Heteronanostructures Based on Reduced Graphene Oxide and Tin Oxide. *Angew. Chem. Int. Ed.* **2012**, *51*, 11053–11057. [CrossRef] [PubMed]
79. Chen, A.; Liu, R.; Peng, X.; Chen, Q.; Wu, J. 2D Hybrid Nanomaterials for Selective Detection of NO_2 and SO_2 Using "Light On and Off" Strategy. *ACS Appl. Mater. Interfaces* **2017**, *9*, 37191–37200. [CrossRef]
80. Hoa, L.T.; Tien, H.N.; Luan, V.H.; Chung, J.S.; Hur, S.H. Fabrication of a novel 2D-graphene/2D-NiO nanosheet-based hybrid nanostructure and its use in highly sensitive NO_2 sensors. *Sens. Actuators B Chem.* **2013**, *185*, 701–705. [CrossRef]
81. Achary, L.S.K.; Kumar, A.; Barik, B.; Nayak, P.S.; Tripathy, N.; Kar, J.P.; Dash, P. Reduced graphene oxide-$CuFe_2O_4$ nanocomposite: A highly sensitive room temperature NH_3 gas sensor. *Sens. Actuators B Chem.* **2018**, *272*, 100–109. [CrossRef]
82. Yamazaki, T.; Okumura, H.; Jin, C.-J.; Nakayama, A.; Kikuta, T.; Nakatani, N. Effect of density and thickness on H_2-gas sensing property of sputtered SnO_2 films. *Vacuum* **2005**, *77*, 237–243. [CrossRef]
83. Yuan, K.-P.; Zhu, L.-Y.; Yang, J.-H.; Hang, C.-Z.; Tao, J.-J.; Ma, H.-P.; Jiang, A.-Q.; Zhang, D.W.; Lu, H.-L. Precise preparation of WO_3@SnO_2 core shell nanosheets for efficient NH3 gas sensing. *J. Colloid Interface Sci.* **2020**, *568*, 81–88. [CrossRef]
84. Liu, H.-H.; Wang, Y.; Jia, A.-P.; Wang, S.; Luo, M.-F.; Lu, J.-Q. Oxygen vacancy promoted CO oxidation over Pt/CeO_2 catalysts: A reaction at Pt–CeO_2 interface. *Appl. Surf. Sci.* **2014**, *314*, 725–734. [CrossRef]
85. Hinokuma, S.; Fujii, H.; Okamoto, M.; Ikeue, K.; Machida, M. Metallic Pd Nanoparticles Formed by Pd−O−Ce Interaction: A Reason for Sintering-Induced Activation for CO Oxidation. *Chem. Mater.* **2010**, *22*, 6183–6190. [CrossRef]
86. Cao, Q.; Hao, S.; Wu, Y.; Pei, K.; You, W.; Che, R. Interfacial charge redistribution in interconnected network of Ni_2P–Co_2P boosting electrocatalytic hydrogen evolution in both acidic and alkaline conditions. *Chem. Eng. J.* **2021**, *424*, 130444. [CrossRef]